Paper 16

Advanced Modelling of Electromagnetic Data

Holtham, E. [1], Marchant, D. [1], McMillan, M. [1], Haber, E. [2]

1. Computational Geosciences Inc., Vancouver, Canada
2. University of British Columbia, Vancouver, Canada

ABSTRACT

In the time since Exploration '07, the quality of collected ground and particularly airborne geophysical data has improved tremendously. New airborne geophysical surveys such as ZTEM are being routinely flown, and induced polarization (IP) measurements are now being extracted from airborne data. Many service providers are also starting to offer drone solutions which show much potential. In addition many advances in both forward modelling and inversion of electromagnetic (EM) data has made the 3D electromagnetic inversion problem tractable, even with large number of sources as seen in airborne surveys. Improved data acquisition combined with advancements in inversion allows the practicing geophysicist working with the data and ultimately making interpretations has the ability to extract the maximum value from these new high quality datasets and models. With a suite of tools to accurately model large EM surveys, a high priority will be placed in the future on integrating the results with other geoscience data and coming up with underlying patterns through machine learning. In this paper, we examine the current state of the art for modelling different 3D EM surveys, and then focus on future opportunities to maximize the value of geophysics within the exploration framework.

INTRODUCTION

As it becomes harder and more expensive to make new world class mineral discoveries, exploration teams must search in increasingly difficult environments particularly under cover such as overburden or glaciation. In such environments, outcrop and geologic information is limited. Remote sensing techniques such as geophysics, have the ability to see through the cover and map lithology, alteration and potentially mineralization. Electromagnetic (EM) techniques are excellent exploration tools because of the large amounts of data and information that can be collected. Unlike potential field methods which are well suited for mapping large scale geologic features and have no depth information, EM data contains sufficient depth information to generate detailed 3D physical property models.

A class of EM data that has seen much attention in recent years is controlled source airborne EM (AEM) techniques. As airborne platforms have advanced and signal to noise ratios have improved, systems are now able to penetrate much deeper than even five years ago. This allows the detection of ore bodies that were previously hidden. Modern systems also collect much more data (for example more time gates for full-waveform airborne time domain systems), as well as three component measurements. Large natural source airborne surveys are also routinely collected that allow large regional structural interpretations even in regions of extreme topography. Ground EM systems have not been left behind and have seen significant improvements in coil design and more widespread adoption of new measurement techniques such as low-noise superconducting sensors. As for direct current resistivity/induced polarization (DC/IP) surveys, many service providers now offer large 3D distributed array data acquisition which allows the earth to be illuminated in a true 3D fashion.

The improvements in data collection techniques leads to more detailed physical property models. As a result, in order to maximize the value extracted from a geophysical dataset, modelling and interpretation techniques must keep pace with the quality of the collected datasets. While simple interpretation techniques such as conductivity-depth imaging (CDI) exist, and are quick tools to determine approximate structure, the generated models do not satisfy the collected geophysical data. As datasets become increasingly complicated, it becomes more difficult to visually inspect the data and make interpretations. Inverting geophysical data generates accurate earth models and ensures that the recovered geophysical model satisfies the data measurements.

1D inversions for both airborne and ground EM are routinely performed and are often satisfactory for many geologic environments. These include standalone 1D inversion packages such as EM1DTM/FM developed by UBC-GIF (Farquharson and Oldenburg, 1993) and 1D laterally constrained software packages such as Workbench (Viezzoli et al, 2008) and VPem1D (Fullagar et al., 2010). Likewise, conductive plate modelling such as Maxwell (EMIT, 2005) MultiLoop (Lamontagne et al., 1988) have been hugely successful for modelling thin plate-like targets. While plate modelling is still often the industry standard for many geologic settings such as VMS deposits, certain approximations made to the physics have motivated hybrid methods such as voxel based parametric approaches. Both 1D and quasi-3D modelling are well suited for a layered earth environments and are quick and easy to run on modern computer hardware. Nonetheless, when the geology becomes complex and 3D in nature, both plate modelling and 1D assumptions can break down and hence full 3D modelling may be required to accurately image the subsurface. These 3D models may eliminate artifacts from 1D assumptions for example and may assist the exploration geoscientist to interpret the complex 3D geologic structures.

In "Proceedings of Exploration 17: Sixth Decennial International Conference on Mineral Exploration" edited by V. Tschirhart and M.D. Thomas, 2017, p. 209–219

With the increased amount of data collected by a modern geophysical survey, 3D inversions are now routinely performed when the setting is appropriate. Since Exploration '07 3D inversion of geophysical data has transitioned from an academic pursuit where a few collected EM soundings were inverted on a very coarse mesh, to the current state of the art where virtually any sized EM survey can be inverted at high resolution using millions of sources. This improvement is due to two main factors. Firstly, computational resources have, and continue to advance in-line with Moore's Law. Algorithms have also improved such that they can now exploit parallel computer architectures, and in some cases even extremely parallel graphical processing units (GPUs). Even a few years ago, inversions were performed on a system with only a few CPU's. Companies such as Amazon have significantly disrupted the computing market with the implementation of cloud computing. Previously a company was required to invest heavily in computer resources if it wanted to perform commercial scale 3D inversions. Today it is possible for any sized company to quickly spin up large computing systems on the cloud using parallel inversion software that is spread across thousands of processors.

This paper is divided into three main sections (advances in 3D EM forward modelling and inversion, examples, and future developments). The focus of the paper is on finite volume type methods as developed by UBC-GIF but other methods such as finite difference (Commer and Newman 2004) finite element (Key and Weiss, 2006, Schwarzbach et al, 2013), and integral equation (Cox et al., 2010) approaches are also being developed as well as quasi-3D techniques such as VPem3D (Fullagar et al., 2015).

ADVANCES IN 3D FORWARD MODELLING AND INVERSION

There have been many advancements in both forward modelling and electromagnetic inversion and a quick review is summarized below. To conduct a forward model simulation, a discretized mesh needs to be constructed to cover the spatial domain of interest. A variety of mesh options exist, each with pros and cons, such as a regular mesh, a semi-structured mesh or an unstructured mesh. For regular meshes, they are easy to build and to view, but they have trouble discretizing complex geologic or topographic features. In addition they can be poorly conditioned and they may require many cells to cover the whole region accurately. For an unstructured mesh, such as using many tetrahedra as is commonly done in finite-element analysis, the meshes are hard to generate, they potentially produce poorly conditioned matrices, but as opposed to regular meshes they are efficient at discretizing geologic features, bathymetry and topography. Semi-structured meshes, such as OcTree (Haber and Heldmann, 2007) represent a compromise between regular mesh and unstructured meshing. These meshes are easier to construct compared to an unstructured orientation but more complicated than regular meshing. In addition, topography and geology can be well discretized but not to the same accuracy level as with tetrahedra. However the system is well-conditioned and the number of mesh cells is relatively low. The examples in this work use semi-structured OcTree meshes, but it is important to know what other options are available. The summary of the different meshes is shown below in Table 1.

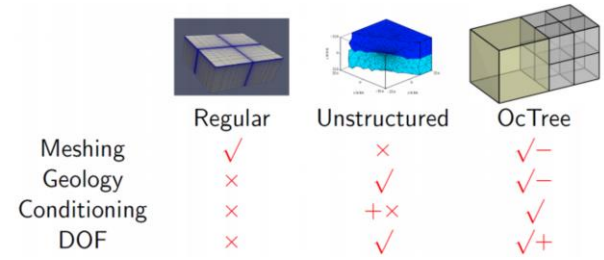

	Regular	Unstructured	OcTree
Meshing	√	×	√−
Geology	×	√	√−
Conditioning	×	+×	√
DOF	×	√	√+

Table 1: Modelling mesh comparison.

One of the most challenging EM surveys to model and invert is controlled source surveys because of the large volume of collected data. Some of the original work on in 3D is from Haber et al. (2007) and Cox and Zhdanov (2008). The problem constitutes finding the spatial distribution of subsurface electrical resistivity which explains the observed data within the limits of the measurement uncertainties. To find such an earth model, one must solve the forward problem, the computation of the predicted data given a resistivity model. When solving the forward problem for AEM surveys, one faces several challenges. The first is the significant number of source locations. Controlled source airborne systems consist of a single moving transmitter and receiver that are flown across the survey area by an aircraft. Typical airborne systems record a new sounding every few metres. For airborne surveys where hundreds to tens of thousands of line kilometres of data are collected, a new sounding every few metres can result in thousands to millions of distinct source locations. Typically, the time to solve the forward problem scales linearly with the number of sources; therefore, it is critical that the forward problem is solved very efficiently. The second difficulty is a problem of scales. AEM surveys can cover large areas and aim at resolving both small and large-scale variations of the subsurface resistivity.

As mentioned above, the chosen mesh needs to cover the whole survey area to consistently account for large-scale features that may influence the data even at a considerable distance from the transmitter location. At the same time, the mesh cell size needs to be fine enough to recover the small-scale features and to reflect the spatial resolution of the data. This easily leads to millions of cells, even with OcTree meshes. While a globally fine mesh is well designed for solving the inverse problem, it is not well suited to solve the forward problem since there are too many cells and each forward solve would be extremely time consuming and computationally demanding. To solve the forward problem for the i^{th} transmitter–receiver pair, the local nature of the measurement only requires that the mesh cells are fine in the vicinity of the transmitter and the receiver.

For numerical efficiency purposes an adaptive meshing approach, as shown in Schwarbach et al., (2013), can be used such that cells close to the transmitter remain fine while cells away from the transmitter region begin to coarsen. See Figure 1 for a 2D slice, and Figure 2 for a 3D view of such a mesh. This adaptive mesh has far fewer cells than the globally fine inverse problem mesh. Reducing the number of cells greatly accelerates the solution of the forward problem since the linear solvers

involved scale superlinearly with the number of unknowns. Using smaller forward problem meshes allows direct solver methods to be used which are efficient when solving with many right hand sides and many time steps. A similar but alternate approach uses a footprint based approach (Cox and Zhdanov, 2008). In this approach, the domain is truncated around the region of interest significantly reducing the computational requirements. Both approaches result in potentially millions of distinct forward problems that can now be solved in parallel and that can exploit modern parallel computer architecture. Apart from the integral equation methods of Cox and Zhdanov (2008), unstructured finite element methods also have been successfully developed (Key and Weiss, 2006; Schwarzbach et al., 2011).

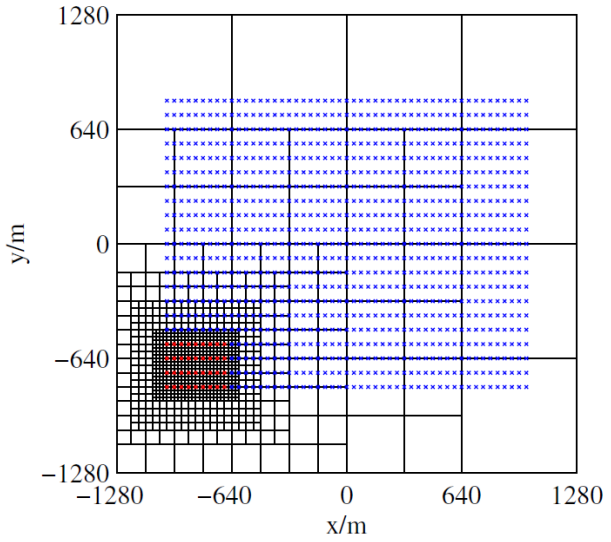

Figure 1: Example plan-view of an adaptive mesh.

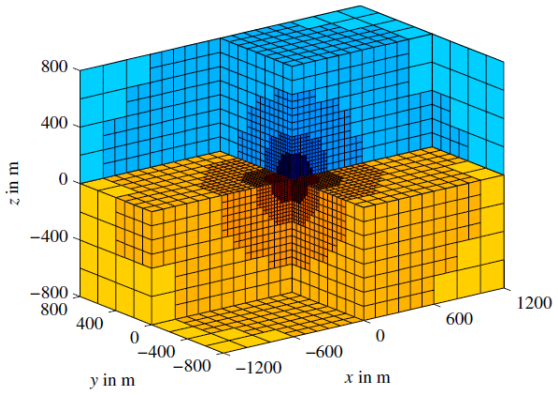

Figure 2: Slice through a 3D mesh optimized for a single source.

Forward Problem Formulation

The forward problem can be formulated as an initial boundary value problem in terms of the magnetic field $H_i(x,t)$,

$$\nabla \times \left(\rho(x)\nabla \times \mathbf{H}_i(\boldsymbol{x},\boldsymbol{t})\right) + \mu(x)\partial \boldsymbol{H}_i(x,t) = \nabla \times (\rho(x)\nabla \times \boldsymbol{H}_{i0}(x)f(t)) \quad (1)$$

For $x \in \Omega$ and $t \in (0, T)$. The initial conditions are given as

$$\boldsymbol{H}_i(x,0) = \boldsymbol{H}_{i,0}(x) \quad (2)$$

and the boundary conditions are

$$\boldsymbol{n} \times (\rho(x)\ \nabla \times \boldsymbol{H}_i(x,t)) = \boldsymbol{0} \quad (3)$$

For $\in \partial\ \Omega$. Here ρ is the electrical resistivity and μ the magnetic permeability. The subscript i indicates the i^{th} transmitter which we model by a current loop which carries a current f *(t)*. For $t \leq 0$, we assume that f (t) = I_0 is constant, giving rise to the magneto-static field $\boldsymbol{H}_{i,0}(x)$ which satisfies

$$\nabla \cdot \left(\mu(x)\boldsymbol{H}_{i,0}(x)\right) = 0 \quad (4)$$

The initial boundary value problem (1) can be discretized in space using the finite volume method on OcTree meshes (Haber and Heldmann, 2007; Horesh and Haber, 2011) and in time using the backward Euler method. This yields a system of linear equations which can be written in compact form as

$$\boldsymbol{A}_i(\boldsymbol{m})\boldsymbol{u}_i = \boldsymbol{b}_i(\boldsymbol{m}) \quad (5)$$

where

$$\mathbf{A}_i(\boldsymbol{m}) = \begin{pmatrix} \mathbf{M}_i + \delta t_1 \mathbf{K}_i(\boldsymbol{m}) & & & \\ -\mathbf{M}_i & \mathbf{M}_i + \delta t_2 \mathbf{K}_i(\boldsymbol{m}) & & \\ & \ddots & \ddots & \\ & & -\mathbf{M}_i & \mathbf{M}_i + \delta t_n \mathbf{K}_i(\boldsymbol{m}) \end{pmatrix} \quad (6)$$

$$\boldsymbol{u}_i = \begin{pmatrix} \boldsymbol{h}_{i,1} \\ \boldsymbol{h}_{i,2} \\ \vdots \\ \boldsymbol{h}_{i,n} \end{pmatrix} \quad \text{and} \quad \boldsymbol{b}_i(\boldsymbol{m}) = \begin{pmatrix} (\mathbf{M}_i + \delta t_1 f_1 \mathbf{K}_i(\boldsymbol{m}))\boldsymbol{h}_{i,0} \\ \delta t_2 f_2 \mathbf{K}_i(\boldsymbol{m})\boldsymbol{h}_{i,0} \\ \vdots \\ \delta t_n f_n \mathbf{K}_i(\boldsymbol{m})\boldsymbol{h}_{i,0} \end{pmatrix}. \quad (7)$$

Here, $\mathbf{M}_i$ is the mass matrix resulting from the finite volume discretization of the time derivative term in Equation 1, and $\mathbf{K}_i$ is the discrete counterpart of the differential operator $\nabla \times (\rho(x)\nabla \times)$. The subscript i indicates that the discretization depends on the i^{th} mesh. $\delta t_1, \ldots, \delta t_n$ are the time step lengths. The vectors $h_{i,1}, h_{i,2}, h_{i,n}$ contain the tangential magnetic field components at the edges of the OcTree mesh at times t_0, t_1, …, t_n. $f_1,\ldots,f_n$ are the values of the current f(t) at times $t_1,\ldots,t_n$. Here the right hand side $\mathbf{b_i}$, depends on the model parameter vector **m** if the source is active during the time stepping, that is if any $f_1,\ldots,f_n$ is nonzero.

The model parameter vector **m** is defined on the global mesh and contains the log-resistivity of each cell of this mesh. To obtain the resistivity for the cells of the i[th] local mesh, we must map from the global mesh to the local mesh. Our solution to this homogenization problem is to take the volume weighted average of the resistivity.

Solving Equation 5 involves solving n systems of linear equations with the system matrices $\boldsymbol{M}_i + \delta t_k \boldsymbol{K}_i\,(\boldsymbol{m})(\mathrm{k} = 1, \ldots, \mathrm{n})$. Since the forward problem is discretized on the small local mesh, the use of sparse direct solvers is possible. These methods are preferable to iterative solvers because the factorizations can be reused for time steps of the same length or multiple sources grouped on the same mesh.

In a standard AEM survey, the time derivative of the vertical magnetic induction $\partial Bz/\partial t$ is measured. By denoting $d_{i,j}^{obs}$ the observed value of $\partial Bz/\partial t$ at the i[th] transmitter location, and the j[th] time channel, the predicted data can be computed from u_i by finite differencing in time and interpolation in space and time. For time channel j and source-receiver pair i, we have

$$d_{i,j}(\boldsymbol{m}) = \boldsymbol{q}_{i,j}^{T}\,\boldsymbol{u}_i = \boldsymbol{q}_{i,j}^{T}[\boldsymbol{A}_i(\boldsymbol{m})]^{-1}\,\boldsymbol{b}_i(\boldsymbol{m}) \tag{8}$$

where the vector $\boldsymbol{q}_{i,i}$ contains the interpolation weights and finite difference coefficients.

Inverse Problem Formulation

To match the predicted and the observed data, we solve a minimization problem and seek a model vector **m*** such that

$$\boldsymbol{m}^* = \operatorname{argmin}\,\phi(\mathbf{m})\,, \tag{9}$$

where $\phi(\mathbf{m}) = \phi_d + \alpha \mathrm{R}(\mathbf{m})$, and the data misfit

$$\phi_d(\mathbf{m}) = \sum_{i=1}^{n_s}\sum_{j=1}^{n_t}\frac{(d_{i,j}(\mathbf{m}) - d_{i,j}^{obs})^2}{(d_{i,j}^{std})^2} \tag{10}$$

n_s denotes the number of sources, n_t the number of measured time channels, $d_{i,j}^{std}$ the standard deviation of the datum $d_{i,j}^{obs}$, α the regularization parameter and R(**m**) a smoothness regularization functional. To minimize the non-linear objection function $\phi(\boldsymbol{m})$ we use the non-linear least squares method and reduce the data misfit until we reach the target data misfit.

EXAMPLES

3D Airborne Time Domain Electromagnetics

The 3D airborne time domain inversion is demonstrated using a SkyTEM example from British Columbia over the Horn River Basin which hosts one of the largest shale gas plays in North America. The huge demand for both water sources and sinks has made the identification and characterization of subsurface aquifers a top priority for those looking to develop the shale gas resource in the Horn River Basin (PRCL, 2011). Figure 3 shows a stratigraphic cross-section of the Horn River Basin with the near surface quaternary channel aquifers. In October 2008, Geoscience BC started the Horn River Basin Aquifer Project with the goal of understanding the hydro-geologic conditions in the area, to investigate potential aquifers in the Horn River Basin, and to quantify and map reservoir capacity and productivity potential. In 2011 the second phase of the project commenced with the goal of continuing the collection and integration of data from deep saline aquifers (PRCL, 2011), as well as examining the use of AEM data to map near-surface groundwater. In April 2011, SkyTEM completed AEM data acquisition over 4 blocks (Stone Mountain - Block 1, Quicksilver - Block 2, EOG - Block 3, Imperial - Block 4). In total over 2400 line-km of AEM and magnetics data were collected using 200 m line spacing. Figure 4 shows the location of the Horn River Basin project and an example of the SkyTEM high moment z-component data is displayed in Figure 5. The data over the Imperial block were inverted in 3D, and Figure 6 shows the 3D resistivity model with a restive cutoff to only show the cells that are less resistive than 15 Ωm. Several interesting conductive features linked to groundwater aquifers are imaged. The inversion result identifies regions 1 and 2 as shown on Figure 6 as potential quaternary channel aquifers. Region 3 is interpreted as the Buckinghorse Shale.

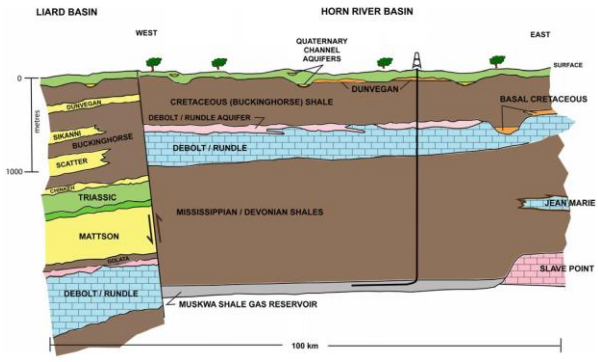

Figure 3: Stratigraphic cross-section of the Horn River Basin and adjacent Liard Basin (figure reproduced from PRCL, 2010).

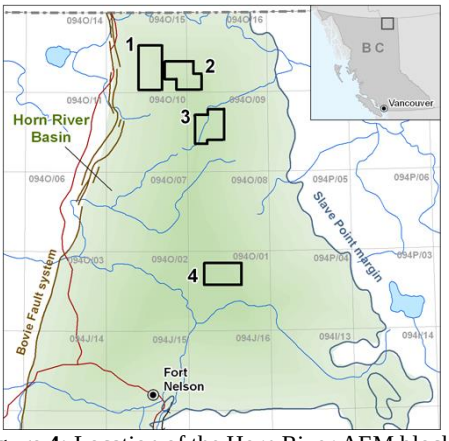

Figure 4: Location of the Horn River AEM blocks.

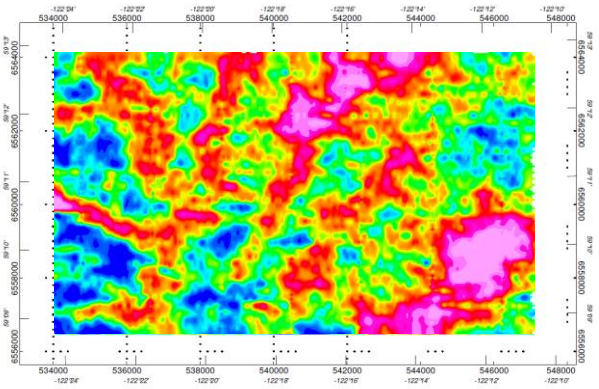

Figure 5: 1.79 ms z-component data from the Imperial block.

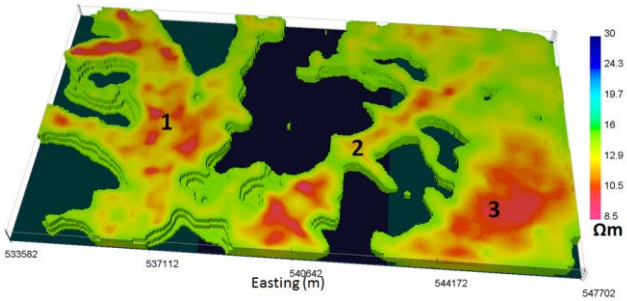

Figure 6: 3D Inversion of SkyTEM data from the Horn River Imperial Block at an elevation of 342 to 292 m above mean sea level (approximately 80 – 130 m below the surface). Regions 1 and 2 are potential quaternary channel aquifers and region 3 is likely the conductive Buckinghorse Shale unit.

3D Airborne Frequency Domain Electromagnetics

The 3D airborne inversion of frequency domain data is shown using RESOLVE data from 2016 over the Committee Bay greenstone belt of Nunavut, Canada. This region, shown broadly in Figure 7, is an active exploration environment for orogenic gold, and the survey was flown to further delineate conductive komatiite units that are known to host mineralization in the area (Kerswill, 1996). The Canadian Arctic is a vast region with existing mines and deposits of many varieties, but exploration potential still abounds. With near-flat topography, airborne surveys can cover large swathes of land with low terrain clearance in this environment. Due to the highly resistive nature of the background rocks, a frequency domain survey was chosen due to its ability to collect high resolution near-surface data at high frequencies. In addition to mapping komatiites and other conductive lithologies of interest such as banded iron formations, the RESOLVE survey also highlights important geologic structures in the region. These faults and fracture networks can provide useful information in order to understand the potential fluid pathways that generated the mineralizing events. In total, 6000 line-km of data were collected with a 200 m line spacing at six frequencies between 400 Hz and 115,000 Hz with five coplanar orientations and one coaxial orientation at 3300 Hz.

Figure 7: Location of Committee Bay greenstone belt in Nunavut, Canada.

The quadrature component of the secondary vertical magnetic field from 8200 Hz is shown in Figure 8. This data map detects many thin linear conductive features in the area in addition to some rounder anomalies, which in this case is usually indicative of shallow lakes. The corresponding inversion of the entire data set is then portrayed in Figure 9 where the conductors highlighted in the data grid are well captured in the inversion. Over 60,000 source locations, each with six frequencies, are incorporated into the inversion using an OcTree mesh with over 2 million cells. The inversion was run on a small in-house cluster consisting of two nodes, with 24 threads each, in less than a day. This represents a dramatic improvement in terms of the size of the inverse problem that can be solved compared to 2007.

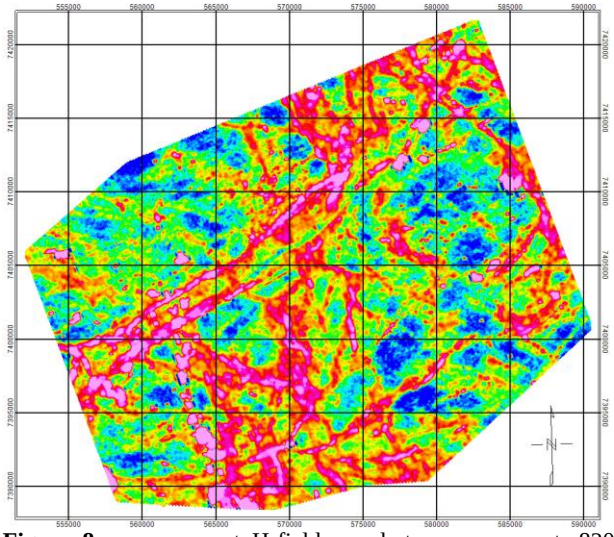

Figure 8: z-component H-field, quadrature component, 8200 Hz.

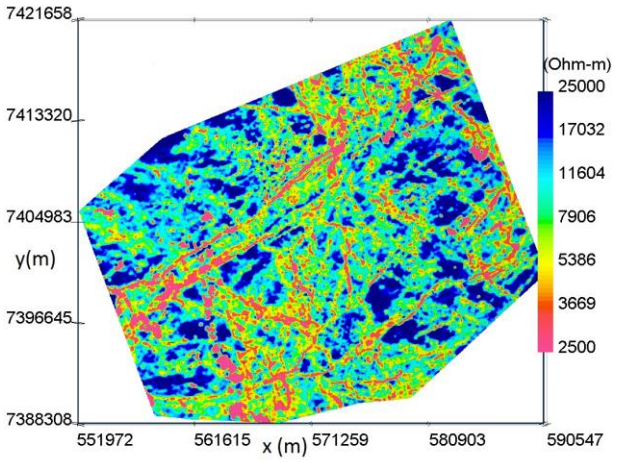

Figure 9: Surface plan view of inversion from 2016 RESOLVE data at Committee Bay, Nunavut.

3D Natural Source Magnetotellurics and ZTEM

Natural source methods are excellent techniques when looking at large-scale structures because of the superior penetration depth. Unlike controlled source methods where the inducing fields exhibits geometric decay, the natural source plane waves penetrate based on the frequency and EM skin depth. For whole earth problems, the magnetotelluric (MT) method has been shown to image up to 500 km. More recently the Z-Axis Tipper Electromagnetic (ZTEM) method developed by Geotech Ltd., has been shown to be effective at mapping large-scale geologic structures. During a ZTEM survey, a helicopter is used to measure the vertical magnetic field over the surface of the earth. The measured data (typically between 30-720 Hz depending on signal strength) relate the measured vertical magnetic field recorded by the helicopter, to the horizontal magnetic field measured at a ground based reference station. Depending on the conductivity of the earth and the EM skin depth, the system can image up to a few kilometres depth in some environments. In addition to the collected ZTEM data, the system also collects aeromagnetic data that can provide additional information for geologic interpretation.

Compared to controlled source methods, inverting natural source data is simple because only two sources need to be modelled (for the two orthogonal field polarizations). Combinations of sparse based ground MT to collect low frequency deep structure, together with high resolution airborne ZTEM is also possible (Holtham and Oldenburg, 2010). While the current ZTEM system only uses a single base station location, incorporating additional base stations may provide some additional information.

3D conductivity and magnetic susceptibility models derived by inverting ZTEM data and the accompanying aeromagnetic data can provide essential information about structures for exploration projects. When inverting the data in 2D, half of the data (usually Tzy) must be ignored because of the 2D assumption. The example below is a 3D ZTEM inversion from a 25,000 line-km dataset collected over extreme topographic relief. The resistive and conductive features of interest are highlighted in Figure 10 while the highly magnetic units are displayed in Figure 11.

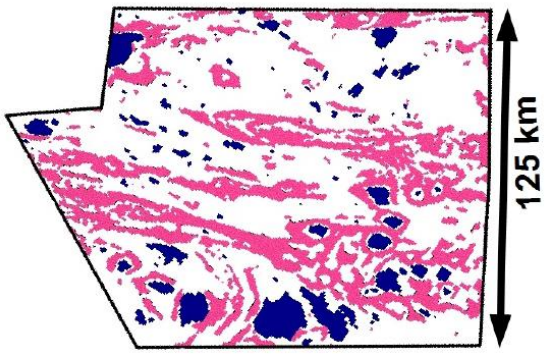

Figure 10: A cropped subsection of a 3D conductivity result obtained by inverting a 25,000 line-km large-scale ZTEM survey. Resistive and conductive cutoffs have been applied to show only the more conductive structures (pink) and more resistive features (blue). The inversion results delineate several interesting structures.

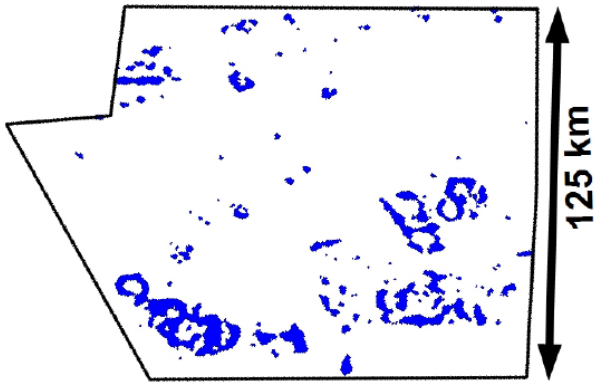

Figure 11: 3D magnetic susceptibility model obtained by inverting the accompanying aeromagnetic data from the ZTEM system. The magnetic susceptibility inversion provides complimentary information to the conductivity inversion, showing that many of the conductive ring structures are also magnetically susceptible.

Hybrid Parametric Inversion

An alternative to conventional voxel-based inversions is a parametric approach, where instead of solving for the conductivity in each mesh cell, the inversion solves for a reduced parameter set that describes the overall conductivity distribution. In large AEM surveys, voxel-based methods such as Oldenburg et al. (2013) can have difficulty in resolving thin targets or sharp boundaries between two contrasting resistivity units. Even with the introduction of compact regularization schemes, voxel inversions can image thin targets as a smeared anomaly, which can pose problems during interpretation or drill targeting. Another issue is the circular nature of the sensitivity from a coincident loop airborne system, which can cause inversion artifacts known as ringing. This can result in

conductive features to be erroneously placed around the true conductive target in a ring-like manner.

Parametric inversions are well researched methods of reducing the parameter space of an inverse problem (Dorn et al., 2000; Zhdanov and Cox, 2013), and can alleviate some of the issues conventional inversions face. Parametric inversions can also be coupled with such methods as level sets (Osher and Sethian, 1988), and together they can solve for the boundary of a conductivity anomaly (Dorn et al., 2000; Aghasi et al., 2011). This enables a computationally efficient method of imaging compact anomalies and sharp boundaries with greater ease. Here we demonstrate a parametric level set approach for time domain AEM, and demonstrate its applicability to both synthetic and field data sets.

The parametric approach searches for one anomaly of interest, either conductive or resistive, in a background of arbitrary conductivity. This background can either be a uniform half-space or a heterogeneous conductivity from apriori information or another inversion algorithm. The conductivity of the anomalous body can be fixed by the user, or the optimal conductivity can be a parameter in the inversion. In the case of a uniform background, the best-fitting background conductivity can also be found. The anomalous conductivity body has the shape of a skewed Gaussian ellipsoid, which is defined by first calculating a smoothly varying function

$$\boldsymbol{\tau} = c - (\mathbf{x} - \mathbf{x_0})^{\mathrm{T}} \mathbf{M} (\mathbf{x} - \mathbf{x_0}) \tag{11}$$

where c represents a positive constant, $\mathbf{x}$ is a vector of observation points in three dimensions, $\mathbf{x_0}$ is vector with spatial coordinates of the anomaly centre, and $\mathbf{M}$ is a 3 x 3 symmetric, positive definite matrix with skewing and rotation parameters. The function is passed to an analytic step-off function s

$$\mathbf{s}(\boldsymbol{\tau}) = \sigma_0 + 0.5\,(1 + \tanh(a\boldsymbol{\tau}))\,(\sigma_1 - \sigma_0) \tag{12}$$

that assigns the conductivity to either a background or anomalous level. The optimization of the inversion follows a Gauss-Newton procedure, where the sensitivity is composed of derivatives of the function $\mathbf{s}$ with respect to the inversion parameters. This optimization scheme is like many conventional voxel-based codes (Oldenburg et al., 2013). The inversion parameters however, are scaled to ensure a well-conditioned Gauss-Newton matrix, and a line search determines an appropriate step length. The program terminates once it has either reached a desired level of convergence, a maximum number of iterations, or when a suitable Gauss-Newton step can no longer be found. If desired, the parametric result can be set as the initial model for a conventional inversion to resolve additional features of interest. This process can be iterated to optimize both the anomalous body and surrounding background features.

The 3D parametric inversion process is demonstrated with a VTEM-35 dataset from Geotech Ltd. over the Caber deposit. Caber is a zinc and copper rich volcanogenic (VMS) deposit in the Matagami camp of the Abitibi Greenstone belt as shown in Figure 12. The deposit itself is thin and steeply dipping to the southwest underneath a layer of conductive overburden. A simplified cross-section through the deposit in Figure 13 shows the thin nature of the mineralized zone, which is traditionally a difficult target to invert for in 3D.

Recent advancements in inversion capabilities have made it possible to image such complex targets as the Caber deposit, and a cross-section through a corresponding 3D hybrid inversion is displayed in Figure 14. The target, modelled through a parametric inversion, is clearly imaged with a steep dip to the southwest below conductive overburden, modelled through a voxel-based inversion. The results agree well with previous geologic mapping and drilling. The inversion shows that the overburden thickens to the northeast and the Caber anomaly dips at roughly an 80° angle compared to the vertical axis. With the same cross-section view, if only the conductive mesh cells are viewed, then the deposit is even more clearly displayed, as in Figure 15. This highlights the usefulness of such a parametric approach to image thin, high contrast targets.

The concept of a parametric inversion is general, as the specific shape of parametrization is open, and the method can be applied to any geophysical data set. For future research, the combination of parametric and voxel-based inversion methods will likely be key in order to model both large scale and small scale features with greater accuracy.

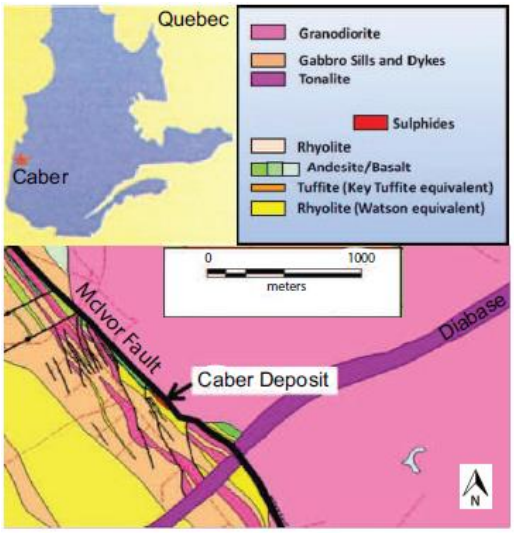

Figure 12: Location and regional geology of Caber deposit.

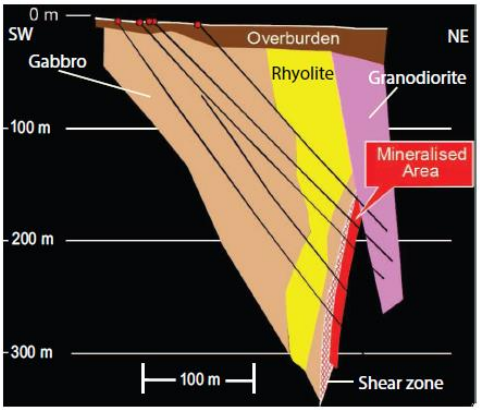

Figure 13: Simplified stratigraphic cross-section through the deposit (modified from Geotech (2012)).

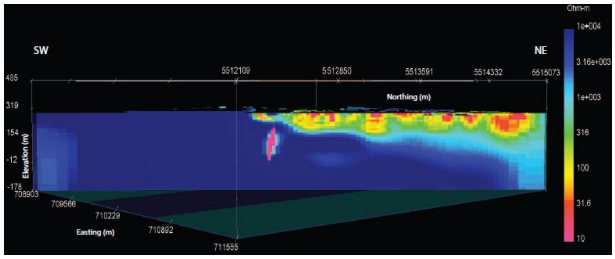

Figure 14: 3D Inversion of VTEM-35 data. The central conductive anomaly is the Caber deposit, which dips to the southwest with a near-vertical dip of 80°.

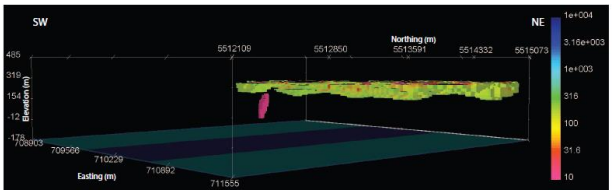

Figure 15: 3D Inversion of VTEM-35 data with only conductive cells less than 175 m shown.

Improved Regularization Options

With inversion being such a non-unique problem, the impact of regularization plays a large and often underappreciated role. The regularization functional R(**m**) has the L2 norm notation

$$R(\mathbf{m}) = \alpha_s \| \mathbf{W}_s(\mathbf{m}-\mathbf{m}_0)\|_2^2 + \alpha_x \| \mathbf{W}_x(\mathbf{m}-\mathbf{m}_0)\|_2^2 + \ldots \\ \alpha_y \| \mathbf{W}_y(\mathbf{m}-\mathbf{m}_0)\|_2^2 + \alpha_z \| \mathbf{W}_z(\mathbf{m}-\mathbf{m}_0)\|_2^2 \qquad (13).$$

Here the α values are user-defined weights that affect the closeness of the model **m** to a reference model $\mathbf{m}_0$ and the overall smoothness of **m**. Diagonal weighting matrices **W** act on particular model cells or boundaries and can be used to inject apriori information into the inversion. However the regularization can incorporate an L1 norm or an approximation to a L0 norm using an Ekblom norm (Ekblom, 1973). This can encourage the recovery of compact targets.

Figure 15 shows an example of the impact the choice of regularization can play. Figure 15a shows the true synthetic model of two conductive dipping units, with values of 0.2 Ωm and 2.0 Ωm respectively. A time-domain AEM survey is simulated over the conductors and three inversions are run with different regularization and fit to the same level. Figure 15b shows an L0-type recovery, Figure 15c depicts an L2 model and Figure 15d displays a parametric inversion model which in itself is a form of regularization. This simple example shows that an L0 norm will encourage compactness compared to an L2 norm, and a parametric formulation in such a setting can produce useful results. Moving forward it will be import to assign an appropriate regularization for the specific problem being solved.

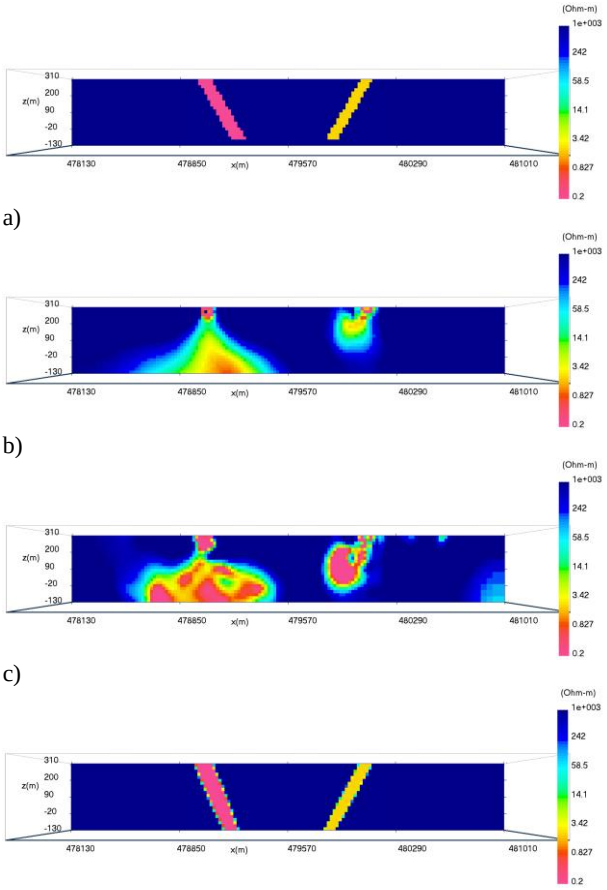

Figure 15: a) True model through two thin conductors. b) L0 model. c) L2 model. d) Parametric model.

Improved Uncertainty Estimates

Ideally the physical property inversion model would be the true earth model; however, for a number of reasons including data noise and modelling errors, the recovered model will have uncertainty. Determining what features in the model are robust and can be trusted, and which features are suspect and should not be relied upon, is critical for the interpretation process. An estimation of model uncertainty is needed. Two schools of thought suggest two different methodologies for uncertainty estimation. Bayesians assume that the apriori information known about the model can be obtained in the form of a probability density function. This assumption leads to many theoretical

understandings and suggests that the probability density function of the model given the data is

$$\pi(\mathbf{m}|\mathbf{d}) \propto \exp\left(-\phi_d(\mathbf{m}) - \beta\phi_m(\mathbf{m})\right).$$

From a Bayesian point of view, the model obtained by the optimization process discussed above is nothing but the model that maximizes the probability density distribution of the model given the data (also called the maximum aposteriori estimate, or MAP).

To estimate the uncertainty of the model, one requires to sufficiently sample from this probability density function, using some kind of Monte-Carlo method. While this is realistic for small scale problems this approach is unrealistic when considering problems with millions of unknowns. Using Monte-Carlo techniques typically requires hundreds of thousands of samples. Since in our case each sample requires the computation of a forward modelling procedure, this approach is unrealistic.

However, while a global approach is not feasible, the local approach is. Linearizing the problem around the solution we obtain that

$$F(\mathbf{m}+\delta\mathbf{m}) \approx F(\mathbf{m}) + \mathbf{J}\delta\mathbf{m} \quad \text{and} \quad \mathbf{J}\delta\mathbf{m} \approx \mathbf{d} - F(\mathbf{m}) = \delta\mathbf{d}$$

which implies that given the linearized problem, the local probability density function for the model perturbation can be written as

$$\pi(\delta\mathbf{m}|\delta\mathbf{d}) \propto \exp\left(-\frac{1}{2}\delta\mathbf{m}(\mathbf{J}^\top\mathbf{W}_d\mathbf{J} + \beta\mathbf{W}^\top\mathbf{W})\delta\mathbf{m} + \delta\mathbf{m}\mathbf{J}^\top\mathbf{W}_d\delta\mathbf{d}\right)$$

This implies that the covariance matrix is nothing but

$$\mathbf{\Sigma}_m = (\mathbf{J}^\top\mathbf{W}_d\mathbf{J} + \beta\mathbf{W}^\top\mathbf{W})^{-1}.$$

and the variance is the diagonal of the matrix. For small scale problems, one can explicitly compute the diagonal of the matrix; however, for large scale problems this is not feasible. In practice, even though the matrix is used at each iteration of the inversion it is never computed explicitly. Only matrix vector products are computed and the matrix is never formed or stored. Nonetheless, a number of techniques can be used to estimate the diagonal of the matrix without estimating the matrix explicitly. In particular, an extension of Hutchinson's trace estimator can be used and in particular, it is straight forward to show that

$$\mathrm{diag}(\mathbf{\Sigma}_m) = \mathbb{E}_{\mathbf{v}}\left(\frac{\mathbf{v}\odot(\mathbf{\Sigma}_m\mathbf{v})}{\mathbf{v}\odot\mathbf{v}}\right).$$

where $\odot$ is the Hadamard product. This identity can be used to approximate the diagonal of the covariance matrix. In particular, if **v** is chosen from a Ranamacher distribution (that is the entries in **v** take the values plus or minus 1), then the vector

$$\mathbf{z} = \frac{1}{n}\sum_{j=1}^{n}\left(\frac{\mathbf{v}_j\odot(\mathbf{\Sigma}_m\mathbf{v}_j)}{\mathbf{v}_j\odot\mathbf{v}_j}\right)$$

is an unbiased approximation to the diagonal of the covariance matrix with the minimal variance. This approximation to the variance can be used in order to roughly estimate the uncertainty in the recovered model. There are a number of points to consider when interpreting uncertainty estimates that are obtained using this methodology. First, it is clear that the uncertainty assumes linearity, however, more importantly, Bayesian methodology is based on the knowledge of the prior. The prior is a comprehensive probability density function that includes all the connections between the model parameters. Such priors are rarely known in practice and therefore the uncertainty estimation is typically optimistic.

One way to obtain a more realistic estimate is to divide the regularization into its smallness term and the smoothness terms, writing

$$\mathbf{\Sigma}_m = \mathbf{J}^\top\mathbf{W}_d\mathbf{J} + \beta_s\mathbf{I} + \beta\mathbf{W}_s^\top\mathbf{W}_s.$$

By defining $\mathbf{H} = \mathbf{J}^\top\mathbf{W}_d\mathbf{J} + \alpha_s\mathbf{I}$, we can use the Woodbury formula

$$(\mathbf{H} + \beta\mathbf{W}_s^\top\mathbf{W}_s)^{-1} = \mathbf{H}^{-1} - \mathbf{H}^{-1}\mathbf{W}_s^\top(\mathbf{I} + \mathbf{W}_s\mathbf{W}_s^\top)^{-1}\mathbf{W}_s\mathbf{H}^{-1}$$

Note that while the second term depends on the choice of prior (that is, the regularization we choose) the first term depends mainly on the data. Therefore, a more conservative estimate of the uncertainty estimate is to evaluate the diagonal of **H**. This is the estimate we tend to use unless some reasonable understanding about the correctness of the prior is evident.

FUTURE DEVELOPMENTS

Improved Data Acquisition

Relative to our oil industry peers, mining geophysical surveys still acquire less data. For example, for offshore oil exploration, companies are routinely collecting large 3D surveys with over 50 receiver lines and source-receiver offsets up to 50 km in length. While EM resolution is hardly as accurate as its seismic counterpart, and mining budgets are hardly that of the oil industry, as a geophysics community we must continue to innovate and devise ways to collect highly quality comprehensive datasets. The quality of the constructed model and the exploration value is directly related to the quality and quantity of the collected data.

New hybrid techniques with innovative combinations of ground and airborne receivers and transmitters should allow for more accurate earth models. While still somewhat of a research topic, recent advances in airborne IP are promising and represent a new dataset that may become routine in years to come. No doubt autonomous drones will also play a major role in the ability to collect more data at a lower cost. To this end, many services providers are already collecting airborne magnetic data from

drone platforms, however we could see drone EM surveys within the coming decade if the payload capacity for drones increases or the weight of EM equipment decreases.

Multi-Physics and Joint Inversion

Electromagnetic data can also be combined in various ways with other geophysical data sets, either through joint or cooperative inversion. Much research has already been done with these techniques, but moving forward the industry can look to combining new data sets that may or may not share a common physical property such as EM/seismic, EM/geology, EM/flow as well as EM surveys that include both surface and borehole measurements. The goal will be to have every inversion working with all the possible information from the area in order to produce the best possible result. This will lead to a greater focus on interpreting all of the multi-physics models. To do this, machine learning will play a prevalent role in harnessing computing power to determine underlying patterns in the models that may not be obvious to the naked eye. This will help the geoscientist interpret the models and will greatly assist with drill targeting.

Constraints

In order for geophysics to become more important in the exploration process, it must have a closer tie with the exploration geology. More research must be focused on incorporating the known geological information of the area into the inversion process. This information could include expected dip information of geologic targets or field or lab physical property measurements. Ideally, down-hole in-field physical property measurements are collected during any drilling campaign in order to better constrain and update subsequent inversions.

There are many tunable parameters in the objective function to constrain the inverse problem, these include applying apriori information to the reference model, as well as applying bounds where borehole information exists. The reference model plays a crucial role in the inversion process as well, because the user is able to specify an estimate of the expected recovered model. The reference model appears many times in the objective function, and therefore the choice of reference model can have large implications for the recovered model. To incorporate borehole resistivity information, an approach is to select all mesh cells that the boreholes intersect and calculate the median and standard deviation of the borehole resistivity values within each discretized cell. Some sort of averaging or statistical approach is needed because of the difference in scale between the boreholes and the mesh, as there are often many resistivity measurements per mesh cell. The median value should work better than the mean because it is less sensitive to outliers. The calculated median resistivity values are then used in the constrained inversion reference model.

Adding upper and lower bound to the model modifies our inversion optimization problem to

$$\begin{aligned} \min \quad & \phi = \phi_d(\mathbf{m}) + \beta\phi_m(\mathbf{m}) \\ s.t. \quad & m^{min} \leq \mathbf{m} \leq m^{max} \end{aligned}$$

and we set the upper and lower bounds for each cell to be some standard deviation above and below the calculated median value. Using this methodology, it is easy for 3D inversions to be constrained by using an appropriate starting and reference model, as well as using lab or borehole information in conjunction with upper and lower bounds.

CONCLUSIONS

Since Exploration '07, both geophysical data acquisition and geophysical inversion methodologies have made majors improvements. With the help of large-scale parallel computing architecture and advanced adaptive meshing techniques, it is now possible to accurately model virtually every EM survey. While this is a step in the right direction, as geophysicists we must continue to work towards not only more accurate physical property models, but also better integration with the geologic exploration models. Looking forward, advances in autonomous drones, a better understanding of IP effects for existing and new airborne systems, a move towards machine learning with resulting multi-physics models and continued improvement with inversion techniques will allow geophysicists to collect and model high quality data, with greater accuracy, at a fraction of traditional acquisition costs.

REFERENCES

Aghasi, A., M. Kilmer, and E.L. Miller, 2011, Parametric Level Set Methods for Inverse Problems: SIAM Journal on Imaging Sciences, 4, 618 – 650.

Cox, L. H., and M.S Zhdanov, 2008, Advanced computational methods of rapid and rigorous 3-D inversion of airborne electromagnetic data: Communications in Computational Physics, 3, 160 – 179.

Commer, M., and G.A. Newman, 2004, A parallel finite-difference approach for 3D transient electromagnetic modeling with galvanic sources: Geophysics, 5, 1192–1202.

Dorn, O., E. Miller, and C. Rappaport, 2000, A shape reconstruction method for electromagnetic tomography using adjoint fields and level sets: Inverse Problems, 16, 1119–1156.

Ekblom, H., 1973, Calculation of linear best Lp approximations: BIT Numerical Mathematics, 13, 292–300.

EMIT, 2005, Maxwell 4.0: Modeling, presentation and visualization of EM and electrical geophysical data.

Farquharson, G., and D.W. Oldenburg, 1993, Inversion of time-domain electromagnetic data for a horizontally layered Earth: Geophysical Journal International, 114, 433–442.

Fullagar, P.K., J. Vrbancich, and G.A. Pears, 2010, Geologically-constrained 1D TEM inversion: ASEG Extended Abstracts 2010.

Fullagar, P., J. Reid, and G. Pears, 2015, Rapid 3D inversion of airborne TEM data from Forrestania, Western Australia: ASEG Extended Abstracts 2015.

Geotech, 2012, VTEM max, http://www.geotech.ca/documents/VTEM_Max_Brochure_Caber.pdf, accessed 25 June 2017.

Haber, E., and S. Heldmann, 2007, An OcTree multigrid method for quasi-static Maxwell's equations with highly discontinuous coefficients: Journal of Computational Physics, 65, 324 - 337.

Haber, E., D.W. Oldenburg, and R. Shekhtman, 2007, Inversion of time domain 3D electromagnetic data: Geophysical Journal International, 132, 1324 - 1335.

Holtham, E., and D.W. Oldenburg, 2010, Three-dimensional inversion of MT and ZTEM data: 80th Annual International Meeting, SEG, Expanded Abstracts, 655-659

Horesh, L., and E. Haber, 2011, A second order discretization of Maxwell's equations in the quasi-static regime on OcTree grids: SIAM Journal on Scientific Computing, 33, 2805 - 2822.

Kerswill, J.A., 1996, Iron-formation-hosted stratabound gold, in Geology of Canadian Mineral Deposit Types, Geology of Canada, 8, 367–382.

Key, K., and C. Weiss, 2006, Adaptive finite-element modeling using unstructured grids: The 2D magnetotelluric example: Geophysics, 71, G291–G299.

Lamontagne, Y., J. Macnae, and B. Polzer, 1988, Multiple conductor modeling using program MultiLoop: 58th Annual International Meeting, SEG, Expanded Abstracts, 237-240.

Oldenburg, D. W., E. Haber, and R. Shekhtman, 2013, Three dimensional inversion of multisource time domain electromagnetic data: Geophysics,78 (1), E47-E57.

Osher, O., and J. Sethian, 1988, Fronts propagating with curvature-dependent speed: algorithms based on Hamilton-Jacobi formulations: Journal of Computational Physics, 79 (1), 12-49.

Petrel Robertson Consulting Ltd. (PRCL), 2010, Horn River Basin Aquifer Characterization Geological Report: Prepared for Horn River Basin Producers Group Geoscience BC, January 2010.

Petrel Robertson Consulting Ltd. (PRCL), 2011, Horn River Basin Aquifer Characterization Project Phase 2 Geological Report: Prepared for Horn River Basin Producers Group Geoscience BC, September 2011.

Schwarzbach, C., E. Haber, and B. Columbia, 2011, Finite element based inversion for electromagnetic problems using stochastic optimization: 81st Annual International Meeting, SEG, Expanded Abstracts, 30, 567 - 572.

Schwarzbach, C., E. Holtham, and E. Haber, 2013, 3D Inversion of Large-scale Time Domain Electromagnetic Data: ASEG Extended Abstracts 2013.

Viezzoli, A., A.V. Christiansen, E. Auken, and K. Sørensen, 2008, Quasi-3D modeling of airborne TEM data by spatially constrained inversion: Geophysics, 73, F105-F113.

Zhdanov, M., and L. Cox, 2013, Multinary inversion for tunnel detection: IEEE Geoscience and Remote Sensing Letters, 10, 5, 1100-1103.